

Article

Description and Classification of Tempering Materials Present in Pottery Using Digital X-Radiography

Alan Nagaya¹, Oscar G. de Lucio^{1,*} , Soledad Ortiz Ruiz² , Eunice Uc González³ , Carlos Peraza Lope³ 
and Wilberth Cruz Alvarado³

¹ Laboratorio Nacional de Ciencias Para la Investigación y la Conservación del Patrimonio Cultural, Instituto de Física, Universidad Nacional Autónoma de México, Apartado Postal 20-364, Ciudad de México 01000, Mexico

² Instituto de Investigaciones Antropológicas, Universidad Nacional Autónoma de México, Circuito Exterior, Ciudad Universitaria, Ciudad de México 04510, Mexico; s.ortiz.ruiz@iia.unam.mx

³ Centro INAH Yucatán, Km. 65 Carretera Progreso, Mérida 97000, Mexico

* Correspondence: olucio@ciencias.unam.mx

Abstract: Archaeological pottery X-radiography is mainly used for two applications: fabric characterization and identification of forming techniques. Both applications require imaging of tempering materials and other additives. With digital X-radiography, it is easy to enhance the image to compute and characterize these materials. In this study, a combination of ImageJ plug-ins such as “threshold”, “analyze particles”, and “fit polynomial” were used to describe tempering materials of a set composed of archaeological pottery sherds. It was found that two different types of tempering materials were used. The first type was characterized by a grain size of less than 0.5 mm and no well-formed particles. In contrast, the second group had a grain size larger than 0.5 mm and well-formed particles.

Keywords: thresholding; X-radiography; digital image analysis



Citation: Nagaya, A.; de Lucio, O.G.; Ortiz Ruiz, S.; Uc González, E.; Peraza Lope, C.; Cruz Alvarado, W. Description and Classification of Tempering Materials Present in Pottery Using Digital X-Radiography. *NDT* **2024**, *2*, 456–473. <https://doi.org/10.3390/ndt2040028>

Academic Editors: Fabio Tosti and Francesco Soldovieri

Received: 20 May 2024

Revised: 18 July 2024

Accepted: 12 October 2024

Published: 16 October 2024



Copyright: © 2024 by the authors. Licensee MDPI, Basel, Switzerland. This article is an open access article distributed under the terms and conditions of the Creative Commons Attribution (CC BY) license (<https://creativecommons.org/licenses/by/4.0/>).

1. Introduction

The properties of pottery can be classified based on their function, firing process, and composition. These properties are determined by examining factors such as the clay matrix, voids, and tempering materials. Various techniques are typically used to analyze these properties, including mineralogical analyses, chemical analyses, and structural characterization. Depending on the characteristic being studied, different methods are used, such as petrography, X-ray diffraction (XRD), X-ray fluorescence (XRF), X-ray photoelectron spectroscopy (XPS), transmission and scanning electron microscopes (TEM and SEM) [1,2].

Some of these techniques are invasive and destructive. However, Heritage Sciences studies require more suitable techniques to provide analysis with non-destructive and non-invasive methods for the study of archaeological pottery; X-radiography is one of the most commonly used procedures. The earliest work using xeroradiography [3] focused on studying several ceramic materials to describe their internal structure and identify tempering materials.

The two main applications of archaeological pottery X-radiography are fabric characterization and identification of forming techniques [4–8]. Both require the imaging of tempering materials and other additives because the material provides insights into mechanical behaviors such as fracture strength and fracture energy, and therefore it could determine its use [9,10]. Describing the size, proportion, type, and general mineralogy of these materials are the main goals for X-radiography; for that reason, the introduction of digital radiography provides new and valuable information owing to digital image processing (DIP) [11].

The use of DIP has spread across different fields in science, aiming to highlight useful information contained in X-rays, considering a digital X-radiography as an $n \times m$ matrix. Different software can be used to manipulate and analyze digital X-radiographies, like

Adobe Photoshop v26.0 with diverse filters in its libraries, such as find edges, adjust levels, smart sharpen, and unsharp-mask [5,12]; Image Pro [13]; Carestream INDUSTREX Digital Viewing Software [14]; and different algorithms; for example, fast bilateral filter (FBF) [15]; methods based on CNNs [16]; and software routines like ShIVA [17].

The software used in this study is ImageJ 1.54f [18]. It is a free-use software based on Java that provides a large number of pre-installed plugins for a large variety of measurements, with the possibility of creating your own algorithms. ImageJ has proven to be helpful in X-radiography analysis for evaluation of bone density [19] and the detection of bucco-palatal/lingual dilacerations [20]; in archaeology, a common application is the DStretch algorithm in rock art enhancement [21], and a review of imaging methodologies using ImageJ can be found in [22]. In this work, we used its tools to analyze and classify different archaeological pottery.

A first approach was made in [23], in which we classified the sherd based on the distribution of its histogram. Now, we improve the methodology based on count particles, a helpful tool used in petrography [2,24], to associate the tempering materials with the different clay classifications. For that, we resume the thresholding method described by [23] to use ImageJ's plug-in analyze particles [25] and improve with shape correction using the plug-in fit polynomial [26].

2. Materials and Methods

2.1. Materials

The same set was analyzed in [23]. There are 201 archaeological pottery sherds from the Mayapán area, 39 from the “Salvamento Arqueológico Carretera Federal Mérida-Campeche” (near the Oxkintok archeological site), and 35 experimental mock-ups; Figure 1 shows some of these objects.

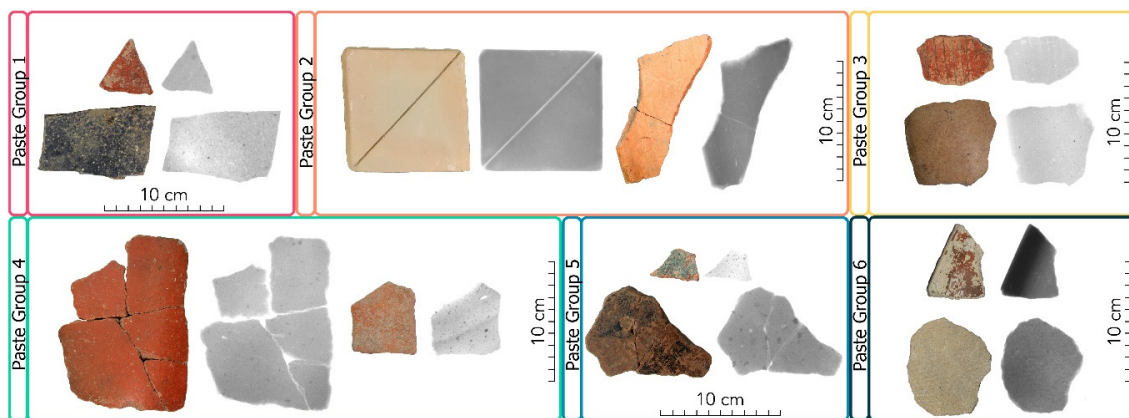


Figure 1. Representative objects of the six different types of clays, according to [23].

Archaeological pottery sherds from the Mayapán region range from the Middle Preclassic to Postclassic periods (700 BC–1500 CE). The pottery was analyzed using the variety type method, as outlined by Smith [27], with additional insights from Peraza et al. [28] and Cruz [29]. Analyzed pottery sherds exhibit slipped surfaces with various decorations such as incisions, spots, bichromy, polychromy, and streaks. Slip quality is dissimilar, presenting flake shedding in some cases. In the case of the Classic period, some of the pieces were unslipped with pastillages, presenting coarse and fine pastes.

During the analysis, characteristic groups from various periods were examined. These included the Postclassic period Tecoh group; the Late Classic period Chum, Chuburna, Muna Slate, Kinich groups; the Early Classic period Hunapchen and Ticumuy groups; the Late Preclassic period Saban and Sierra groups; and the Middle Preclassic period Chuhuinta, Loche, and Ek Maben groups, and Juventud, which extends to the Early Classic in use.

Archaeological sherds from the “Salvamento Arqueológico Carretera Federal Mérida-Campeche” were found in various domestic contexts and span from the Middle Preclassic to the Terminal Classic periods, including the representative groups Juvetud, Dzudzuquil, Chunchinta Piral, Maxcanu, Sierra, Saban, Águila, Timucuy, Kochol, and Ticul.

The purpose of using mock-ups manufactured by the potters was to provide us with easy-to-analyze objects. They were flat, with standard dimensions, and made following traditional recipes. These mock-ups were also measured with different spectroscopy techniques and other image techniques.

The sherds were classified into six different types of clay through the histogram analysis [23], in which we adjusted a Lorentzian function and classified respect to parameters ω and x_c , the first one related to homogeneity and the second one related to material characteristics. The resulting data are presented in Table A1.

Paste 1 and Paste 4 are the groups with the largest number of objects. They are characterized by having an intermediate ω value, meaning they have intermediate material homogeneity. The histograms of objects from Paste 1 tend to shift towards the white and have a nonsymmetric distribution, with the appearance of shoulders on the right. On the other hand, the objects from Paste 4 tend to shift towards black and have a nonsymmetric distribution, with the appearance of shoulders on the right.

For Paste 2, Paste 3, and Paste 6, small ω values indicate high material homogeneity and symmetrical distributions. The primary distinction among these groups lies in the location of the maximum gray level. Paste 3 has the lowest radiological density, while Paste 6 has the highest. Paste 5 exhibits the lowest homogeneity, with a nonsymmetrical distribution and shoulders on both sides.

2.2. Methodology

The overall procedure (see Figure 2) for determining the tempering materials present in the pottery pastes was as follows:

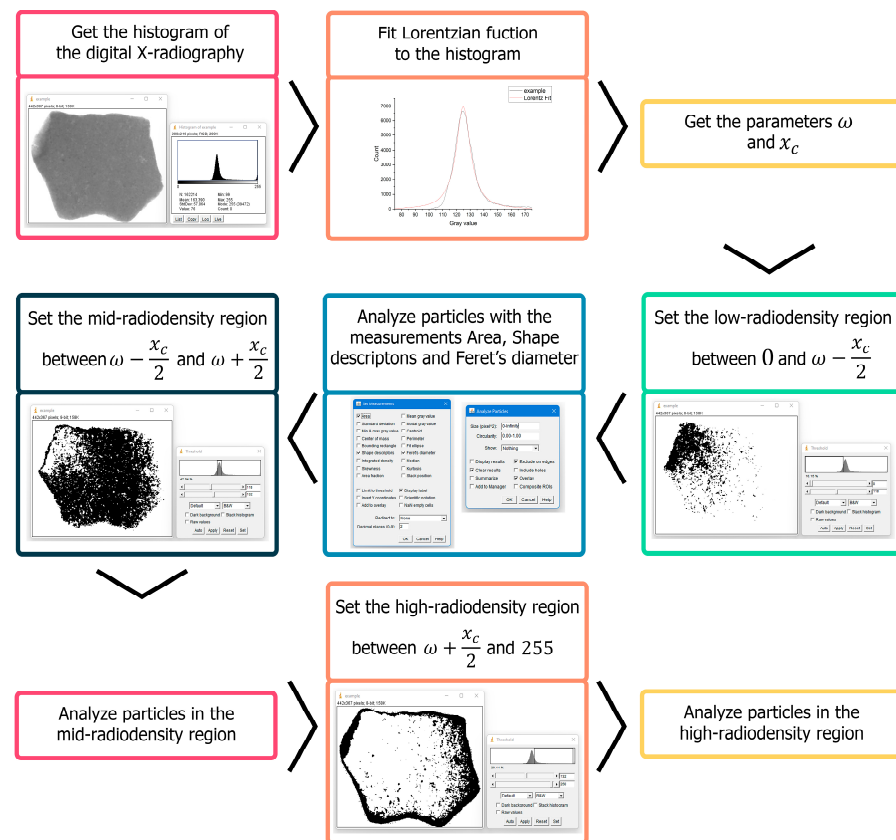


Figure 2. Flowchart of the methodology for analyzing tempering materials.

Radiographic images were acquired by using a digital radiography system, where the distance to the object and detector was fixed, and parameters such as voltage and filament current were adjusted to improve contrast; to optimize acquisition times, different pottery sherds were included in the same image, keeping a record of their position. An aluminum stair with known dimensions, which had previously been characterized, was employed to provide a normalization between images with different acquisition conditions.

The resulting images were then transformed to positive, where white and black correspond to 255 and 0, respectively, and analyzed by describing their histogram. Depending on the information present in the histogram, the analysis could be straightforward (for flat and homogeneous sherds) or require an additional step of image improvement, where effects due to volumetric distortions of the studied object were removed. As a result, a Lorentzian distribution is fitted to the corresponding pixel distribution shown in the histogram.

Employing the parameters resulting from the Lorentzian fit, a threshold can be defined, and segments corresponding with different radio opacities can be described in the radiographic image. Thus, the actual region where the particles present in the pottery paste, corresponding with tempering material, can be defined and analyzed.

Further details on the different methodology steps are described in the following sub-sections.

2.2.1. X-Radiography Acquisition

The X-radiographs were taken with the digital radiography equipment previously characterized in [23]. The system is based on an X-ray source POSKOM XM-40BT that produces X-rays in a voltage range between 40 and 100 kV and a current range between 0.4 and 100 mA·s, in addition to a flat panel detector Vidisco Imager FlashX Pro that has an effective area of analysis of 43.2×34.2 cm. Radiographies were recorded under the following experimental conditions: voltage was set at 50 kV and filament current at 40 mA·s; the distance from the X-ray source to the detector (DRD) was set at 1.00 ± 0.05 m. The flat panel detector provides a $144 \mu\text{m}/\text{px}$ measured resolution and produces 11-bit negative images. After the acquisition, all resulting images were processed to convert the grayscale to positive.

2.2.2. ImageJ Application

ImageJ 1.54d was used. Figure 2 presents the flowchart describing the methodology for analyzing tempering materials. The first step is obtaining the histogram and describing its behavior. The material behavior is described with the different distributions of the histogram; each maximum in the histogram distribution is related to a ceramic paste [23].

If it only shows one maximum, the *Lorentz fit* is applied directly (Figure 3a); in this case, the object is flat, and the radiography behavior is homogeneous. Nevertheless, due to object shape or *sgraffito*, the histogram of X-radiography presents two (or more) local maximums. When the second maximum is generated by *sgraffito* or pottery decoration, it is not possible to enhance using the *fit polynomial* plug-in (Figure 3b); nevertheless, the second maximum is caused by pottery shape, such as thickening or thinning, and it is possible to enhance the digital image with the *fit polynomial* plug-in (Figure 3c).

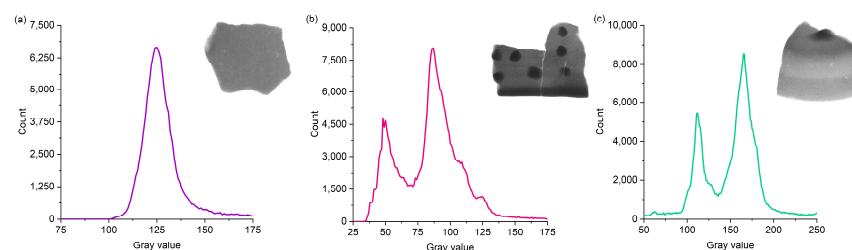


Figure 3. Representative histograms of three sherds. (a) Single maximum histogram, in which we apply directly the Lorentzian adjust. (b) Histogram with two maxima, in which, due to the sherd decoration, it is not possible for the plot profile enhancement. (c) Histogram with two maxima, in which it is possible the plot profile enhances due to the second maximum being caused by the sherd shape.

The fit polynomial plug-in was originally developed to correct the illumination of microscopy images [26]. We can apply the plug-in because, in understanding X-radiography, for the positive, the thickening is presented by the decrease of gray values, and the thinning is presented by the growth of gray values; in other words, the thickening in a digital image can be understood as shadows and thinning can be understood as lights. The plug-in has three conditions, x , y , and xy ; the conditions must be iterated to choose the fit polynomial that only presents one maximum in the histogram distribution and that maximizes the ω parameter in the Lorentzian adjust (Figure 4). With this enhancement, the histogram distribution is homogenized, allowing us to highlight the tempering materials hidden in the sherd geometry (Figure 5).

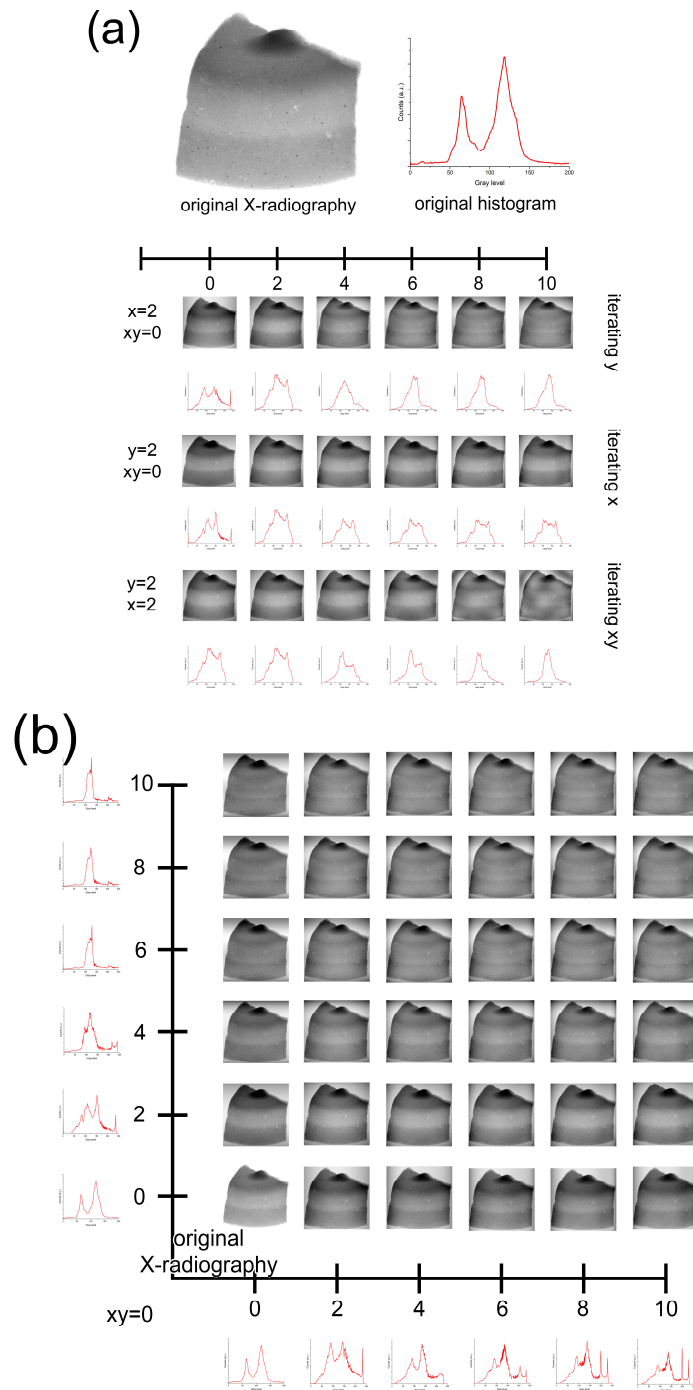


Figure 4. (a) Iteration of the parameters x , y , and xy , with the other two fixed. (b) Iteration of x and y parameter with xy fixed.

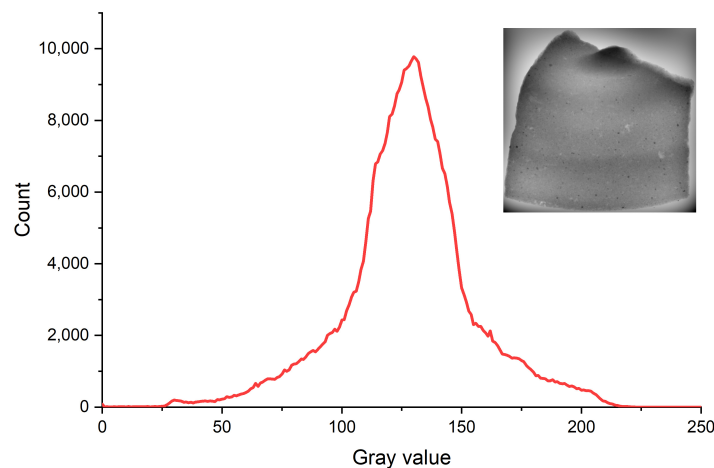


Figure 5. Histogram of sherds presented in Figure 3c after fit polynomial enhancement with parameters $x = 6$ $y = 5$ $xy = 5$.

With the Lorentzian adjust, a threshold was applied in three different regions: The low radiodensity region between 0 and $x_c - \frac{\omega}{2}$; in this region, the thresholding highlights the areas with thinness; the medium radiodensity region between $x_c - \frac{\omega}{2}$ and $x_c + \frac{\omega}{2}$; this region represents most of the pixels in the radiography and it is linked to matrix clay; and the high radiodensity region between $x_c + \frac{\omega}{2}$ and 255; in this region the thresholding highlights the regions with thickness. With this thresholding, analyze particles was used to get the parameters of Area, Feret's diameter, and Shape descriptors.

2.2.3. Analysis of Parameters

The three parameters used to describe the tempering materials are area, to determine the proportion of tempering materials in the pottery; Feret's diameter, to describe the grain size [30] (the tempering material's grain size is less than 5 mm [31,32]; due to the flat panel resolution, this distance is 35 px (5.04 mm)); and circularity, aspect ratio, and roundness, to describe the shape of the tempering material.

The distinction between the tempering materials from the clay matrix was made considering the grain size, with the thresholding highlighting all the regions with gray levels in the range defined and corresponding with the clay matrix. Consequently, grain sizes larger than 35 px with low roundness and circularity are considered a clay matrix, since the clay matrix does not have a defined shape, and since it represents the most significant part of pottery, the clay matrix has to be large, and the parameters of shape are irrelevant with areas less than 5 px^2 .

2.2.4. Digital Microscopy Images

Microscopical side views were acquired with a USB-microscope Dino-Lite model AM4815ZTL-EDGE to describe surface details and possibly identify structures and tempering materials present in the paste. The images were recorded with DinoCapture 2.0 using the EDOF algorithm.

3. Results and Analysis

Figure 6 (top) shows two objects with different tempering materials highlighted in red. The tempering materials were discriminated from clay matrix according to grain size.

The analyze particles method allows us to identify two different tempering materials. Figure 6a shows an object in which the tempering materials are predominantly not well-formed, i.e., with a parameter of roundness low at 0.5, and grain size between 0 and 0.5 mm, with high predominant silt-size inclusions. The second type of tempering materials are shown in Figure 6b, which are predominantly well-formed, with a roundness parameter high at 0.7 and grain size high at 1 mm.

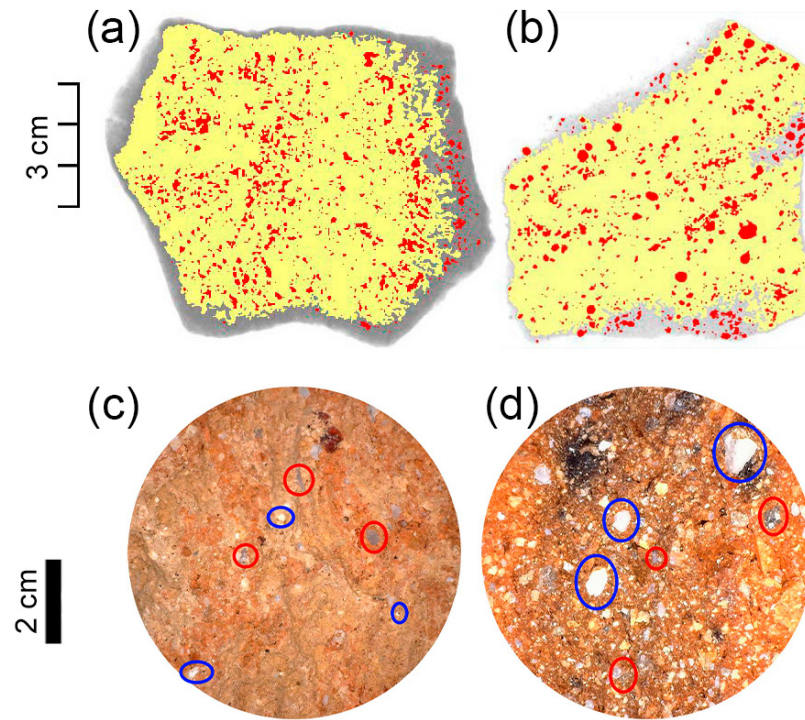


Figure 6. (Top) Highlight of clay matrix (yellow) and tempering materials (red). (a) This object has 6.42% of tempering materials with respect to the total pottery, and they are not well-formed. (b) This object has 5.5% tempering materials with respect to the total pottery and predominantly has well-formed inclusions. (Bottom) Microscopy side view of the pottery, with red circles marking the calcite and blue circles indicating the possibly silicate particles. (c) No well-formed tempering materials object. (d) Well-formed tempering materials object. See Appendix B for complementary information.

A second classification of pottery was performed, considering the different types of tempering materials. Figure 7 shows the frequency of different sherds. It was found that different types of tempering materials were used in the same clay matrix. The most common type of tempering material (labeled as 1 in Figure 7) was in 82.10% of total objects; the second type (labeled as 2 in Figure 7) appears only in selected objects with very low frequency (17.90%). Four groups only have a single kind of tempering material, and two groups share tempering materials.

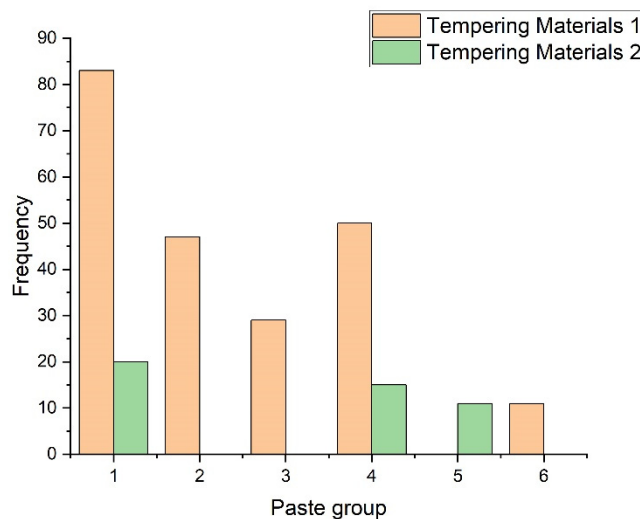


Figure 7. Frequency of paste groups and tempering materials.

Paste 2, Paste 3 and Paste 6 do not present the second type of tempering materials that agree with our previous description of this pottery. These Paste groups have symmetrical distributions and high material homogeneity. In the case of Paste 1 and Paste 4, the second type of tempering materials could explain the appearance of the shoulder on the right. In these groups, only a small percentage contains the second type of tempering materials. In the case of Paste 5, the presence of a second type of tempering material contributed to the low homogeneity. It is worth mentioning that all objects in the group contained the same kind of tempering material.

The parameters described in these objects provide information about the purpose of the pottery. The grain size affects the final characteristics of pottery; for example, in the calcite case, a small grain size produces lime spalling [33–35]; the roundness is inversely related to toughness [9] and volume fraction, such as the case of quartz, and a higher concentration of these tempering materials in the final product achieves higher toughness [36]. This is in addition to other characteristics that require other techniques; for instance, using quartz increases the heat conductivity, contrary to calcite, which reduces the heat conductivity [37] but requires the correct mineral characterization. Because of that, this method does not substitute traditional techniques but provides a fast, noninvasive, and nondestructive way to find interesting objects to analyze.

4. Conclusions

Our work has led to the development of a nondestructive method that provides detailed information on the material characteristics of pottery pastes, focusing on the analysis of tempering materials. This method, based on basic physics concepts such as the attenuation of X-rays in matter, systematically describes the pixel distributions in digital radiographic images using mathematical algorithms. This represents a significant improvement over previous contributions, which focused solely on the description of radiographic images. Compared with microscopical observations, the developed method provides information without sampling, making it a noninvasive and nondestructive methodology. This method allows us to analyze a great number of objects without sampling them and with minimal supervision. And the parameters resulting from our analysis, such as grain size or Feret's diameter and shape descriptions, that have not been previously considered a result of this kind of radiographic image analyses, thus provide insights into tempering materials in a variety of pottery that can be compared with those resulting from more invasive and typical methods such as thin section petrographic analysis or microscopies, which usually require sample preparation and destruction of the studied objects.

The method proposed here complements conventional techniques for the characterization of tempering materials. The description of these allows the classification of different sherds and additionally provides information for the use of other techniques, such as the location of different particles using XRF or XRD, or else the election of representative sherds using petrography, to identify the materials. In this work, it was possible to distinguish two kinds of tempering materials; one of them appears to be of more common occurrence, corresponding with highly homogeneous pastes, with radiography histograms highly symmetrical, while the other kind appears only in few of the studied objects, where the pastes are typically inhomogeneous and produce radiography histograms with a superposition of different pixel distributions.

The information generated by this analysis allows us to provide insights into the pottery manufacturing techniques employed by the ancient Maya civilization, which, in a future work, along with an elemental and molecular characterization and a correlation with mineralogical determination techniques, could provide answers to specific archaeological questions, such as provenance, existence of material reutilization, material source locations, or innovations performed over the different archaeological horizons.

This work has a potentially significant impact due to further applications of the developed method (since, at this point, we showed only a small amount of application

examples), which, along with an archeological or archaeometric interpretation, will soon produce results that are of interest to different research areas.

Author Contributions: A.N.: Writing—original draft, Methodology, Software, Formal analysis, Investigation. O.G.d.L.: Writing—review and editing, Methodology, Visualization, Investigation, Funding acquisition, Project administration. S.O.R.: Writing—review and editing, Methodology, Archaeological Investigation, Archaeological Findings Interpretation. E.U.G. and C.P.L.: Archaeological Research Manager, Writing—review, Archaeological Investigation. W.C.A.: Writing—review, Archaeological Investigation. All authors have read and agreed to the published version of the manuscript.

Funding: This research was funded by CONAHCYT, grant number CF 2019 No. 731762 and by DGAPA-PAPIIT grant number IG-100424. Experimental work was possible thanks to the support by CONAHCYT grants LN293904, LN299076, LN314846, LN315853.

Data Availability Statement: Images and resulting calculations are available upon request.

Acknowledgments: Experimental results were possible due to the support granted by Laboratorio Nacional de Ciencias para la Investigación y Conservación del Patrimonio Cultural (LANCIC-IF). We acknowledge the technical support of J. Cañetas and A. Mitrani as well as the constructive discussion and guidance of Teresa Pi Puig.

Conflicts of Interest: The authors declare no conflicts of interest.

Appendix A

Table A1. List of studied objects, associated main parameters, paste and tempering material classification results with temporality.

Object	Temporality	Paste Type	Tempering Material Type
C001	Middle Preclassic	1	1
C002		4	1
C003	Middle Preclassic	1	1
C004	Middle Preclassic	4	2
C005	Middle Preclassic to Early Classic	1	1
C006	Middle Preclassic to Early Classic	4	1
C007	Middle Preclassic	1	1
C008	Middle Preclassic	4	1
C009		4	1
C010	Middle Preclassic	1	1
C011	Middle Preclassic	4	1
C012	Middle Preclassic	4	1
C013	Middle Preclassic	1	1
C014	Middle Preclassic	1	1
C015	Middle Preclassic	1	1
C016	Middle Preclassic	1	1
C017	Middle Preclassic	1	2
C018	Middle Preclassic	1	2
C019	Early Classic	1	2
C020	Middle Preclassic	4	2
C021	Middle Preclassic	4	1
C022	Middle Preclassic	1	1

Table A1. *Cont.*

Object	Temporality	Paste Type	Tempering Material Type
C023	Middle Preclassic	1	1
C024	Middle Preclassic	3	1
C025	Middle Preclassic	2	1
C026	Middle Preclassic	1	1
C027	Middle Preclassic	1	1
C028	Middle Preclassic	1	1
C029		2	1
C030	Middle Preclassic	4	1
C031	Middle Preclassic	1	1
C032	Middle Preclassic	1	1
C033	Middle Preclassic	4	1
C034	Middle Preclassic	1	1
C035	Middle Preclassic	3	1
C036	Middle Preclassic	1	1
C037	Middle Preclassic	1	1
C038	Middle Preclassic	4	1
C039	Middle Preclassic	4	1
C040		1	1
C041	Middle Preclassic	2	1
C042	Middle Preclassic	4	2
C043	Middle Preclassic	1	2
C044	Middle Preclassic	1	2
C045	Middle Preclassic	1	1
C046	Middle Preclassic	1	2
C047		1	1
C048	Middle Preclassic	1	1
C049	Middle Preclassic	2	1
C050	Middle Preclassic	2	1
C051	Middle Preclassic	3	1
C052	Middle Preclassic	1	1
C053	Middle Preclassic	1	1
C054	Middle Preclassic	1	1
C055	Middle Preclassic	1	1
C056	Middle Preclassic	4	2
C057	Middle Preclassic	1	1
C058	Middle Preclassic	1	2
C059	Middle Preclassic	1	1
C060	Middle Preclassic	1	1
C061	Middle Preclassic	1	2
C062	Middle Preclassic	2	1

Table A1. *Cont.*

Object	Temporality	Paste Type	Tempering Material Type
C063	Middle Preclassic	1	1
C064	Middle Preclassic	4	1
C065	Middle Preclassic	1	2
C066	Middle Preclassic	5	2
C067	Middle Preclassic	3	1
C068	Middle Preclassic	1	2
C069	Late Preclassic	1	1
C070	Late Preclassic	1	1
C071	Late Preclassic	6	1
C072	Late Preclassic	1	1
C073	Late Preclassic	4	2
C074	Late Preclassic	1	1
C075	Late Preclassic	1	1
C076	Middle Preclassic	1	1
C077	Late Preclassic	4	2
C078	Late Preclassic	1	1
C079	Late Preclassic	3	1
C080	Late Preclassic	1	1
C081	Late Preclassic	3	1
C082	Late Preclassic	3	1
C083	Late Preclassic	2	1
C084	Late Preclassic	2	1
C085	Late Preclassic	1	1
C086	Late Preclassic	4	1
C087	Late Preclassic	1	1
C088	Late Preclassic	4	1
C089	Late Preclassic	1	1
C090	Late Preclassic	1	1
C091	Late Preclassic	4	1
C092	Late Preclassic	1	1
C093	Late Preclassic	1	1
C094		3	1
C095	Middle Preclassic	1	1
C096	Middle Preclassic	1	1
C097	Middle Preclassic	1	1
C098	Middle Preclassic	1	1
C099	Middle Preclassic	1	1
C100	Late Preclassic	3	1
C101	Early Classic	6	1
C102	Late Preclassic	3	1
C103	Late Preclassic	3	1

Table A1. *Cont.*

Object	Temporality	Paste Type	Tempering Material Type
C104	Late Preclassic	3	1
C105		5	2
C106	Early Classic	4	1
C107	Early Classic	1	1
C108	Early Classic	1	1
C109	Early Classic	1	1
C110	Early Classic	4	1
C111	Late Preclassic	3	1
C112		3	1
C113	Early Classic	1	2
C114		1	1
C115	Late Preclassic	3	1
C116		4	1
C117	Late Preclassic	1	1
C118	Early Classic	1	1
C119	Early Classic	2	1
C120	Early Classic	4	1
C121	Late Preclassic	5	2
C122	Early Classic	1	1
C123	Early Classic	1	1
C124	Early Classic	4	2
C125	Early Classic	1	2
C126	Early Classic	1	1
C127	Early Classic	4	1
C128	Early Classic	1	1
C129	Early Classic	1	1
C130	Early Classic	1	1
C131	Early Classic	1	2
C132	Early Classic	1	2
C133	Early Classic	1	2
C134	Early Classic	3	1
C135	Early Classic	2	1
C136	Late Classic	1	1
C137	Late Classic	1	1
C138	Late Classic	1	1
C139	Late Classic	1	2
C140	Late Classic	1	1
C141	Late Classic	1	1
C142	Late Classic	1	1
C143	Early Classic	1	1
C144	Early Classic	5	2

Table A1. *Cont.*

Object	Temporality	Paste Type	Tempering Material Type
C145		6	1
C146	Late Classic	6	1
C147	Late Classic	4	1
C148	Late Classic	4	1
C149	Terminal Classic	1	1
C150	Terminal Classic	1	1
C151	Terminal Classic	1	2
C152	Late Classic	5	2
C153	Late Classic	1	1
C154	Late Classic	1	2
C155	Late Classic	1	1
C156	Late Classic	4	1
C157	Late Classic	4	1
C158	Late Classic	3	1
C159	Late Classic	2	1
C160		1	1
C161	Late Classic	1	1
C162	Late Classic	1	1
C163	Terminal Classic	1	2
C164	Late Classic	6	1
C165	Late Classic	2	1
C166	Late Classic	3	1
C167	Terminal Classic	1	2
C168	Terminal Classic	1	1
C169	Late Classic	3	1
C170		4	1
C171	Late Classic	4	1
C172	Late Classic	4	1
C173	Late Classic	4	1
C174	Late Classic	4	1
C175	Late Classic	1	1
C176	Late Classic	4	1
C177	Late Classic	1	1
C178	Late Classic	1	1
C179	Postclassic	2	1
C180	Postclassic	2	1
C181	Postclassic	2	1
C182	Postclassic	1	1
C183	Postclassic	1	1
C184	Late Classic	1	1
C185	Late Classic	2	1

Table A1. *Cont.*

Object	Temporality	Paste Type	Tempering Material Type
C186	Late Classic	6	1
C187	Late Classic	2	1
C188		3	1
C189	Early Classic	5	2
C190	Early Classic	5	2
C191	Early Classic	6	1
C192	Middle Preclassic	3	1
C193	Middle Preclassic	3	1
C194		6	1
C195		6	1
C196		4	1
C197		4	1
C198		3	1
C199		6	1
C200		6	1
C201		5	2
D001	Middle Preclassic	4	2
D002	Middle Preclassic	4	2
D003	Middle Preclassic	4	1
D004	Middle Preclassic	4	2
D005	Middle Preclassic	4	2
D008	Late Preclassic	6	1
D009	Late Preclassic	3	1
D013	Late Preclassic	3	1
D014	Early Classic	3	1
D016	Early Classic	3	1
D017	Early Classic	4	1
D019	Early Classic	3	1
D020	Early Classic	3	1
D022	Early Classic	4	1
D023A	Early Classic	4	1
D025	Early Classic	4	1
D025	Early Classic	4	1
D027	Early Classic	4	1
D028	Late Classic	4	2
D029	Late Classic	4	2
D030	Late Classic	4	1
D031	Late Classic	4	1
D031	Late Classic	4	1
D033	Late Classic	4	1

Table A1. Cont.

Object	Temporality	Paste Type	Tempering Material Type
D033	Late Classic/Terminal Classic	4	2
D035	Late Classic/Terminal Classic	4	2
D036	Late Classic/Terminal Classic	4	1
D036	Late Classic/Terminal Classic	4	1
D039	Late Classic/Terminal Classic	4	1
D041	Late Classic/Terminal Classic	4	1
D042	Late Classic/Terminal Classic	6	1
D043	Late Classic/Terminal Classic	6	1
D044	Late Classic/Terminal Classic	3	1
D046	Late Classic/Terminal Classic	3	1
D047	Late Classic/Terminal Classic	3	1
D048	Late Classic/Terminal Classic	3	1
D049	Terminal Classic	3	1
D050	Terminal Classic	4	1
D051	Terminal Classic	5	2
E001	Mock-ups	2	1
E002	Mock-ups	2	1
E003	Mock-ups	2	1
E004	Mock-ups	2	1
E005	Mock-ups	2	1
E006	Mock-ups	2	1
E007	Mock-ups	2	1
E008	Mock-ups	2	1
E009	Mock-ups	2	1
E010	Mock-ups	2	1
E011	Mock-ups	2	1
E012	Mock-ups	2	1
E013	Mock-ups	2	1
E014	Mock-ups	2	1
E015	Mock-ups	2	1
E016	Mock-ups	2	1
E017	Mock-ups	2	1
E018	Mock-ups	2	1
E019	Mock-ups	2	1
E020	Mock-ups	2	1
E021	Mock-ups	2	1
E022	Mock-ups	2	1
E023	Mock-ups	2	1
E024	Mock-ups	2	1
E025	Mock-ups	2	1
E026	Mock-ups	2	1

Table A1. Cont.

Object	Temporality	Paste Type	Tempering Material Type
E027	Mock-ups	2	1
E028	Mock-ups	2	1
E029	Mock-ups	2	1
E030	Mock-ups	2	1
E031	Mock-ups	2	1
E032	Mock-ups	2	1
E033	Mock-ups	2	1
E034	Mock-ups	2	1
E035	Mock-ups	2	1

Appendix B

We used SEM analysis with a Hitachi TM3030 Plus and Bruker Quantax 75 for elemental analysis and mapping to identify the mineral composition without using petrography. Figure A1a shows the measurement area mentioned in Figure 6d. Figure A1b displays the map of Ca concentration, and Figure A1c displays the map of Si concentration. Both elements cluster in certain regions, with the Ca regions corresponding to white dots and the Si regions corresponding to gray regions, described as silicate particles in Section 3.

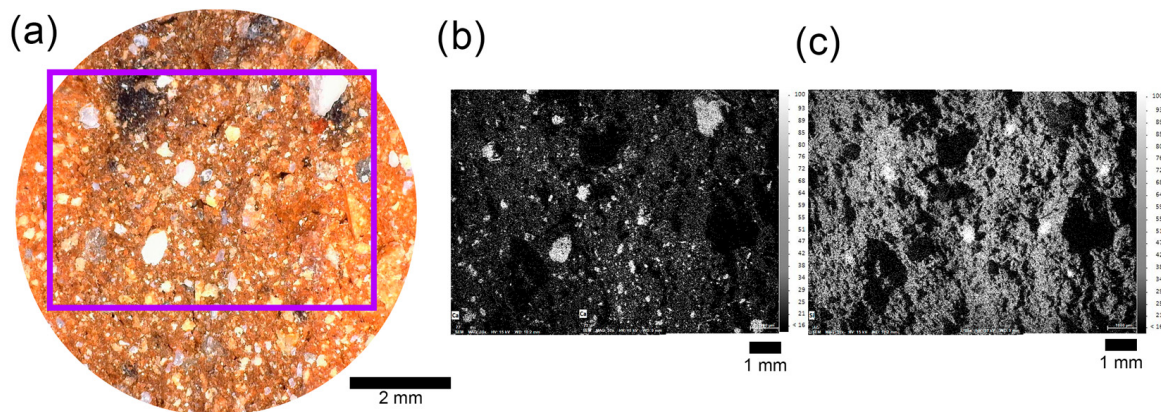


Figure A1. (a) Microscopy side view of the pottery (Figure 6) with the SEM-analysis area highlighted. (b) SEM elemental mapping of Ca. (c) SEM elemental mapping of Si.

This result supports the idea that these materials are added to the clay matrix. Figure A1c clearly shows that the Si is spread throughout all pottery, caused by the clay matrix, but the concentration differs in tempering material aggregates, highlighting these ones.

We conducted petrographic analysis on specific pieces using conventional methods. In Figure A2, the thin section of object D005 is displayed, revealing the presence of the second type of tempering material. The section exhibits well-formed calcite particles, as detailed in Section 3. However, quartz particles are not identifiable by radiographic analysis in this sample since the resolution is higher than 0.144 mm in a flat panel.

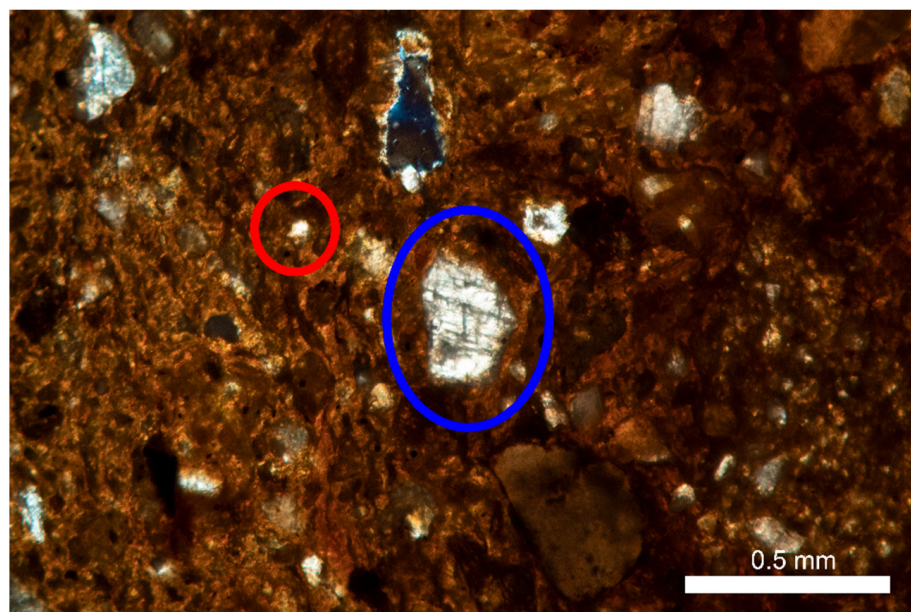


Figure A2. Thin section NX 30 mm of object D005. The blue circle indicates the calcite, with a grain size of 0.3 mm, and the red circle indicates quartz, with a grain size of less than 0.1 mm, so this is not distinguishable in the radiography image due to flat panel resolution.

References

1. Rice, P. *Pottery Analysis: A Sourcebook*; University of Chicago Press: Chicago, IL, USA, 2006; pp. 309–446.
2. Quinn, P.S.; Zhang, S.; Xia, Y.; Li, X. Building the terracotta army: Ceramic craft technology and organisation of production at qin shihuang's mausoleum complex. *Antiquity* **2017**, *91*, 966–979. [[CrossRef](#)]
3. Titterton, P.F. Certain bluff mounds of western jersey county, Illinois. *Am. Antiq.* **1935**, *1*, 6–46. [[CrossRef](#)]
4. Ikeoka, R.A.; Appoloni, C.R.; Scorzelli, R.B.; Santos, E.D.; Rizzutto, M.D.A.; Bandeira, A.M. Study of ancient pottery from the brazilian amazon coast by edxrf, pixe, xrd, mössbauer spectroscopy and computed radiography. *Minerals* **2022**, *12*, 1302. [[CrossRef](#)]
5. McCarthy, B. Examination of processing techniques in cultural heritage objects with radiography. *Am. Ceram. Soc. Bull.* **2020**, *99*, 24–29.
6. Norris, D.; Watson, O. Illuminating the imperceptible, researching mina'i ceramics with digital imaging techniques. *J. Imaging* **2021**, *7*, 233. [[CrossRef](#)]
7. Okońska-Bulas, M.; Mikołajska, A. Wheel-made pottery of the przeworsk culture in the light of digital radiography examinations. Preliminary study of vessels from the microregion to the east of the lower raba river. *Acta Archaeol. Carpathica* **2022**, *57*, 115–142. [[CrossRef](#)]
8. Thér, R. Ceramic technology. How to reconstruct and describe pottery-forming practices. *Archaeol. Anthropol. Sci.* **2020**, *12*, 172. [[CrossRef](#)]
9. Müller, N.S.; Vekinis, G.; Day, P.M.; Kilikoglou, V. The influence of microstructure and texture on the mechanical properties of rock tempered archaeological ceramics. *J. Eur. Ceram. Soc.* **2015**, *35*, 831–843. [[CrossRef](#)]
10. Sterba, J.H.; Mommsen, H.; Staeinhauser, G.; Bichler, M. The influence of different tempers on the composition of pottery. *J. Archaeol. Sci.* **2009**, *36*, 1582–1589. [[CrossRef](#)]
11. Berg, I. Looking through pots: Recent advances in ceramics x-radiography. *J. Archeol. Sci.* **2008**, *35*, 1177–1188. [[CrossRef](#)]
12. Soares Batista, S.; Panzarella, F.K.; Tavano, O.; Filho, A.M.; Junqueira, J.L.C. Image adjustments on digital panoramic radiographs using adobe photoshop CS3 software. *RSBO Rev. Sul-Bras. Odontol.* **2013**, *10*, 394–401. [[CrossRef](#)]
13. Lu, W.; Zhang, N.; Ren, N.; Ding, Z.; Yang, F.; Hu, Q.; Li, J. Bubble-induced formation of new intermetallic compounds in an al–mn alloy during heating observed by synchrotron radiography. *Materialia* **2021**, *15*, 1000991. [[CrossRef](#)]
14. Martins, A.; Davis, E.; Kwartler, T. Max ernst's woman, old man, and flower (1923–1924): Four paintings in one revealed by technical imaging. *Heritage* **2021**, *4*, 2224–2236. [[CrossRef](#)]
15. Yahaghi, E.; Garcia, J.A.M.; Movafeghi, A. Fracture and internal structure detection of ceramic objects using improved digital radiography images. *J. Cult. Herit.* **2020**, *44*, 152–162. [[CrossRef](#)]
16. Gozes, O.; Greenspan, H. Bone structures extraction and enhancement in chest radiographs via cnn trained on synthetic data. In Proceedings of the 2020 IEEE 17th International Symposium on Biomedical Imaging (ISBI), Iowa City, IA, USA, 3–7 April 2020; pp. 858–861. [[CrossRef](#)]

17. Greene, A.F.; Hartley, C.W.; Dupuy, P.N.D.; Chinander, M. The digital radiography of archaeological pottery: Program and protocols for the analysis of production. *J. Archaeol. Sci.* **2017**, *78*, 120–133. [[CrossRef](#)]
18. Schneider, C.; Rasband, W.; Eliceiri, K. Nih image to imagej: 25 years of image analysis. *Nat. Methods* **2012**, *9*, 671–675. [[CrossRef](#)]
19. Geiger, M.; Blem, G.; Ludwig, A. Evaluation of imagej for relative bone density measurement and clinical application. *J Oral J. Oral Health Craniofacial Sci.* **2016**, *1*, 12–21. [[CrossRef](#)]
20. Satir, S.; Buyukcavus, M.H.; Orhan, K. A novel approach to radiographic detection of bucco-palatal/lingual dilacerations: A preliminary study with imagej. *Proc. Inst. Mech. Eng. Part H J. Eng. Med.* **2021**, *235*, 1310–1314. [[CrossRef](#)]
21. Harman, J. Using decorrelation stretch to enhance rock art images. *Am. Rock Art Res. Assoc. Annu. Meet.* **2005**, *28*, 1–4.
22. Saunders, D.; Collmann, R.; Borda, A. Reflectance transformation imaging and imagej: Comparing imaging methodologies for cultural heritage artefacts. In *Electronic Visualisation and the Arts (EVA 2017)*; BCS Learning & Development: Swindon, UK, 2017.
23. Nagaya, A.; Tlacuilo, R.; de Lucio, O.; Ortiz, S. Desarrollo de un método de clasificación de pastas cerámicas basado en el análisis de imágenes de radiografía digital. *Boletín La Soc. Geológica Mex.* **2024**, *76*, A101223. [[CrossRef](#)]
24. Reedy, C.L.; Anderson, J.; Reedy, T.J. Quantitative porosity studies of archaeological ceramics by petrographic image analysis. *MRS Online Proc. Libr.* **2014**, *1656*, 9–14. [[CrossRef](#)]
25. Sbalzarini, I.F.; Koumoutsakos, P. Feature point tracking and trajectory analysis for video imaging in cell biology. *J. Struct. Biol.* **2005**, *151*, 182–195. [[CrossRef](#)] [[PubMed](#)]
26. Kuru, K. Optimization and enhancement of H&E stained microscopical images by applying bilinear interpolation method on lab color mode. *Theor. Biol. Med Model.* **2014**, *11*, 9. [[CrossRef](#)]
27. Smith, R.E. *The Pottery of Mayapan Including Studies of Ceramic Material from Uxmal, Kabah, and Chichen Itza*; Peabody Museum of Archaeology and Ethnology, Harvard University: Cambridge, MA, USA, 1971.
28. Peraza Lope, C.; Masson, M.A.; Cruz Alvarado, W.; Russell, B.W. Effigy Censer and Figurine Production at the Postclassic Maya City of Mayapan, Mexico. *Anc. Mesoam.* **2023**, *34*, 455–475. [[CrossRef](#)]
29. Cruz Alvarado Wilberth, A. Distribución y Cronología de sitios Arqueológicos del Centro-sur de Yucatán. Bachelor's Thesis, Universidad Autónoma de Yucatán, Mérida, México, 2010.
30. Tomaszewski, P.E. The uncertainty in the grain size calculation from X-ray diffraction data. *Phase Transit.* **2013**, *86*, 260–266. [[CrossRef](#)]
31. Virto, I.; Moni, C.; Swanston, C.; Chenu, C. Turnover of intra- and extra-aggregate organic matter at the silt-size scale. *Geoderma* **2010**, *156*, 1–10. [[CrossRef](#)]
32. Sheppard, P.; Walter, R.; Dickinson, W.; Felgate, M.; Ross-Sheppard, C.; Azemard, C. A solomon sea interaction sphere. In *The Lapita Cultural Complex in Time and Space: Expansion Routes, Chronologies and Typologies*; Archeologia Pasifika, Institut d'archaeologie de la Nouvelle-Caledonie et du Pacific: Noumea, New Caledonia, 2015; pp. 63–80.
33. Eramo, G. Ceramic technology: How to recognize clay processing. *Archaeol. Anthropol. Sci.* **2020**, *12*, 164. [[CrossRef](#)]
34. Maritan, L.; Ganzarolli, G.; Antonelli, F.; Rigo, M.; Kapatza, A.; Bajnok, K.; Coletti, C.; Mazzoli, C.; Lazzarini, L.; Vedovetto, P.; et al. What kind of calcite? Disclosing the origin of sparry calcite temper in ancient ceramics. *J. Archaeol. Sci.* **2021**, *105358*, 129. [[CrossRef](#)]
35. Allegreta, I.; Pinto, D.; Giacomo, E. Effects of grain on the reactivity of limestone temper in a kaolinitic clay. *Appl. Clay Sci.* **2016**, *126*, 223–234. [[CrossRef](#)]
36. Kilikoglou, V.; Vekinis, G.; Maniatis, Y.; Day, P.M. Mechanical performance of quartz-tempered ceramics: Part I, strength and toughness. *Archaeometry* **1998**, *40*, 261–279. [[CrossRef](#)]
37. Allegretta, I.; Eramo, G.; Pinto, D.; Hein, A. The effect of temper on the thermal conductivity of traditional ceramics: Nature, percentage and granulometry. *Thermochim. Acta* **2014**, *581*, 100–109. [[CrossRef](#)]

Disclaimer/Publisher's Note: The statements, opinions and data contained in all publications are solely those of the individual author(s) and contributor(s) and not of MDPI and/or the editor(s). MDPI and/or the editor(s) disclaim responsibility for any injury to people or property resulting from any ideas, methods, instructions or products referred to in the content.